

# A Tunable Despeckling Neural Network Stabilized via Diffusion Equation

Yi Ran, Zhichang Guo, Jia Li\*, Yao Li, Martin Burger, Boying Wu

**Abstract**—Multiplicative Gamma noise remove is a critical research area in the application of synthetic aperture radar (SAR) imaging, where neural networks serve as a potent tool. However, real-world data often diverges from theoretical models, exhibiting various disturbances, which makes the neural network less effective. Adversarial attacks work by finding perturbations that significantly disrupt functionality of neural networks, as the inherent instability of neural networks makes them highly susceptible. A network designed to withstand such extreme cases can more effectively mitigate general disturbances in real SAR data. In this work, the dissipative nature of diffusion equations is employed to underpin a novel approach for countering adversarial attacks and improve the resistance of real noise disturbance. We propose a tunable, regularized neural network that unrolls a denoising unit and a regularization unit into a single network for end-to-end training. In the network, the denoising unit and the regularization unit are composed of the denoising network and the simplest linear diffusion equation respectively. The regularization unit enhances network stability, allowing post-training time step adjustments to effectively mitigate the adverse impacts of adversarial attacks. The stability and convergence of our model are theoretically proven, and in the experiments, we compare our model with several state-of-the-art denoising methods on simulated images, adversarial samples, and real SAR images, yielding superior results in both quantitative and visual evaluations.

**Index Terms**—Convolutional neural network, adversarial attack, synthetic aperture radar image despeckling, diffusion equation, multiplicative Gamma noise.

## I. INTRODUCTION

**S**YNTHETIC aperture radar (SAR), an active remote sensing system, is an indispensable tool that can be applied to disaster monitoring [1], land cover classification [2], and object detection [3]. However, SAR images are often contaminated by speckle noise due to scattering and coherence phenomena [4]. Therefore, denoising preprocessing of SAR images is crucial to further analysis or application. The acquisition process of SAR images can be modeled as [5]

$$f = u\eta \quad (1)$$

where  $u : \Omega \subset \mathbb{R}^2 \rightarrow \mathbb{R}$  represents the potential clean image,  $f$  represents the observed image, and  $\eta$  represents the multiplicative Gamma noise following the Gamma distribution with

mean value equals to one. The probability density function related to the multiplicative Gamma noise is given by:

$$P(\eta) = \frac{L^L}{\Gamma(L)} \eta^{L-1} e^{-L\eta} \mathbf{1}_{\{\eta \geq 0\}}$$

where  $\mathbf{1}_{\{\eta \geq 0\}}$  is the indicator function defined on  $\{\eta \geq 0\}$ , and  $L$  represents the number of looks. The current multiplicative denoising methods can be roughly divided into traditional methods and deep learning methods.

Early approaches primarily relied on spatial filtering techniques, such as the Lee filter [6], Kuan filter [7], Frost filter [8], Gamma maximum a posteriori (MAP) filter [9], and the nonlocal means filter [10]. Subsequently, variational methods gained popularity due to their notable stability and computational efficiency. The AA model [11] performed multiplicative denoising by minimizing a functional composed of a total variation (TV) regularizer and a fidelity term obtained by MAP. This model had significant influence, though its fidelity term becomes non-convex when  $2f < u$ . To address this issue, the globally convex SO model [12] utilized a logarithmic transformation to convert multiplicative noise into additive noise, thereby facilitating its removal. An adaptive total variation (TV) model was introduced in [13], which innovatively introduced the concept of gray value indicator functions for the adaptive removal of multiplicative noise. It is well known that every functional corresponds to a partial differential equation (PDE), and the use of anisotropic diffusion equations for denoising had become increasingly prevalent among researchers. Recently, a doubly degradation framework incorporating a gray value indicator function had been proposed in [14], which used degenerate characteristics in the areas of zero gray values ( $u = 0$ ) and edges ( $|\nabla u| = \infty$ ) to control the diffusion speed and thus effectively remove noise. Numerous PDE-based models had been developed under this framework [15]–[18], yielding remarkable results.

With the development of computational power, restoration effects of deep learning had significantly surpassed traditional methods. One of the earliest attempts to utilize neural networks for the removal of multiplicative Gamma noise was SAR-CNN [19]. SAR-CNN employed logarithmic transformation and incorporated the DnCNN module [20] to perform multiplicative denoising. IDCNN was proposed in [21], which divided noisy images by the estimated noise and adopted the structure of residual networks to remove the multiplicative noise. However, these models are traditional neural networks, which are difficult to interpret. To integrate both the power of neural networks and the high interpretability of traditional methods, strategies like Plug-and-Play and Unrolling had

Yi Ran, Zhichang Guo, Jia Li, Yao Li, and Boying Wu are with the School of Mathematics, Harbin Institute of Technology, 150001 Harbin, China (e-mail: 21b912025@stu.hit.edu.cn; mathgzc@hit.edu.cn; jli@hit.edu.cn; yaoli0508@hit.edu.cn; mathwby@hit.edu.cn).

Martin Burger is with the Computational Imaging Group and Helmholtz Imaging, Deutsches Elektronen-Synchrotron DESY, 22607 Hamburg, Germany and Fachbereich Mathematik, Universität Hamburg, 20146 Hamburg, Germany (e-mail: martin.burger@desy.de).

\* is the corresponding author.

been introduced. Models under the Plug-and-Play framework had been successfully applied to SAR denoising [22]–[25]. Unlike Plug-and-Play, the concept of unrolling suggests that traditional iterative algorithms can be unfolded into neural networks. SAR-RDCP employed the half-quadratic splitting method to handle an energy functional, with a neural network serving as a regularizer, and unrolled it into the network [26]. A similar strategy was utilized in [27] to develop a SAR image denoising network, integrating TV loss and Charbonnier loss functions [7]. Zhou et al. proposed a deep unrolling network based on ADMM to effectively achieve denoising [28].

Owing to the absence of ground truth labels for real SAR images, the denoising networks are trained on simulated datasets derived from the idealized model (1). Nonetheless, the distribution of real-world data are often different from the simulated data. Natural disturbances, including rain, snow, and fog, are inevitable and directly impair the performance of trained neural networks [29]. Specifically, the most detrimental perturbations to neural networks are often identified via adversarial attack strategies, for which numerous methods have been developed [30]–[33]. Moreover, adversarial attacks demonstrate a universal characteristic, that most general networks are highly susceptible [34]. The denoising-PGD attack algorithm [33], specifically designed for image denoising, demonstrates remarkable transferability across neural networks, allowing a single adversarial sample to compromise multiple models. In summary, a neural network with resistance to adversarial attacks exhibits enhanced adaptability to real-world data. Consequently, the ability of a neural network to defense adversarial attacks serves as an effective criterion for evaluating its robustness.

Numerous strategies have been employed to improve the robustness of neural networks. A straightforward approach is adversarial training, which improves network robustness by incorporating adversarial examples into the training process [35], [36], such as Lipschitz learning [37], [38]. However, computing the Lipschitz constant of a neural network is an NP-hard problem [39]. The strategies [40]–[42] for constraining the Lipschitz constant at each layer or activation introduce significant computational overhead and may reduce the robustness of neural networks [43]. A recent two-stage method, IP-NDE, incorporates neural network priors into the coefficients of diffusion equations to enhance robustness [44]. Nonetheless, the primary stabilizing factor in this two-stage method lies in the diffusion equation itself, which does not directly modify the robustness of the neural network. Encouragingly, the success of [44] inspires further investigation into utilizing the dissipative properties of diffusion equations to enhance neural network stability.

This paper aims to develop a robust neural network that matching state-of-the-art performance on non-adversarial samples, while also excelling in adversarial samples for effective real-world applications. Inspired by the unrolling algorithm and the stability of diffusion equations, we propose a tunable regularization network utilizing a linear diffusion equation to enhance model robustness.

## II. RELATED WORK

### A. Integrated methods of model-driven and data-driven

The goal of SAR image denoising is to recover the original image  $u$  from observed data  $f$ , as described by (1).

From a probabilistic perspective, Maximum A Posteriori Probability (MAP)  $p(u|f)$  is a popular estimator. Applying Bayes' theorem, we obtain

$$\hat{u} = \operatorname{argmax}_u p(u|f) = \operatorname{argmin}_u -\log(p(f|u)) - \log(p(u))$$

which could be abstracted as a general variational model

$$\hat{u} = \operatorname{argmin}_u \{\mathcal{F}(u, f) + \lambda\mathcal{R}(u)\} \quad (2)$$

where  $\mathcal{F}(u, f)$  represents the fidelity term, and  $\mathcal{R}(u)$  denotes the regularization term. Under the assumption of (1), the AA model [11] employs a total variation regularizer [45] to suppress multiplicative noise

$$\inf_{u \in BV(\Omega), u > 0} \int_{\Omega} \left( \log u + \frac{f}{u} \right) + \lambda \|u\|_{TV} \quad (3)$$

and proved the existence of minimizer of (3) in the space of bounded variation function  $BV(\Omega)$  theoretically.

The ADMM technique [46] decouples the MAP estimation problem (2) into a forward model and a prior model:

$$\hat{u}^k = \operatorname{argmin}_u \left\{ \mathcal{F}(u, f) + \frac{\beta}{2} \|u - \hat{v}^{k-1} + \hat{z}^{k-1}\|_2^2 \right\} \quad (4)$$

$$\hat{v}^k = \operatorname{argmin}_v \left\{ \lambda\mathcal{R}(v) + \frac{\beta}{2} \|\hat{u}^k - v + \hat{z}^{k-1}\|_2^2 \right\} \quad (5)$$

$$\hat{z}^k = \hat{z}^{k-1} + \hat{u}^k - \hat{v}^k \quad (6)$$

which provides a bridge for the connection between neural network prior and theoretical forward process. The plug-and-play strategy [47] replaced the (5) by an already trained network to improve the denoising performance.

Unlike the plug-and-play approach, unrolling algorithms decompose traditional iterative methods into layers of a neural network, enabling end-to-end training. The use of unrolling algorithms in multiplicative denoising is increasing recently [26]–[28]. This technique has been shown to enhance the effectiveness and efficiency of image denoising processes, especially when dealing with complex noise patterns like multiplicative noise [48]. In the SAR-RDCP model [26], a neural network  $\mathcal{D}_{\theta}(u)$  is employed to replace the regularizer in (3), and the model was unrolled into a network following the application of the half-quadratic splitting method.

### B. Stability and adversarial attack

Adversarial attacks exploit minor perturbations in input data to significantly degrade the original performance of a network [30], [49]. In this paper, we use adversarial attacks to test the robustness of the model to improve the adaptability of our model to real data.

Recently, a specialized attack on the denoising algorithm, L2-denoising-PGD method has been proposed [33], which minimize the negative L2-norm between the output of the network and the clean image to complete the attack.

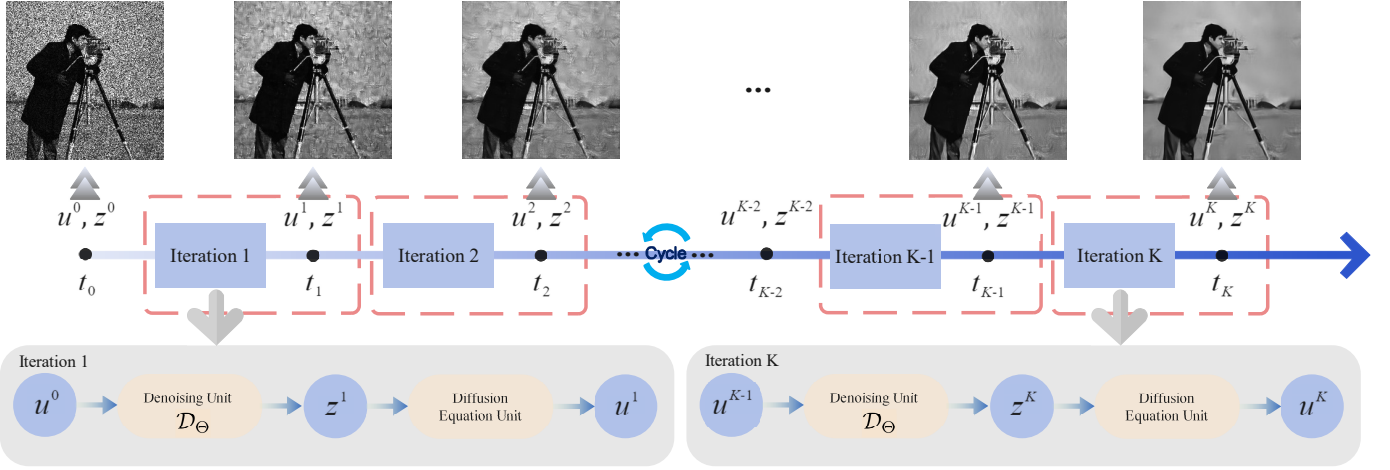


Fig. 1. framework of our model

For a denoising network  $\mathcal{D}_\theta(f)$ , where  $f$  is generated by applying multiplicative Gamma noise to the clean image  $u$ , the adversarial attack can be formulated as

$$\max_{\varepsilon} \mathcal{L}(\mathcal{D}_\theta(f + \varepsilon), u) \quad \text{s.t.} \quad \|\varepsilon\|_2 \leq \epsilon$$

where  $\mathcal{L}$  is the loss function and  $\epsilon$  is the threshold of the perturbation. The process of generating adversarial samples under the L2-denoising-PGD strategy is

$$f^{t+1} = f^t + \alpha \text{sign}(\nabla_f \mathcal{L}(\mathcal{D}_\theta(f), u))$$

where  $f^t$  is the adversarial sample at iteration  $t$ ,  $\alpha$  represents the iterating step and  $\text{sign}(\cdot)$  is the sign function. To maintain a sufficiently small perturbation, values are clipped to remain within the range  $[-\epsilon, \epsilon]$ . It was also noted that adversarial samples generated by the L2-denoising-PGD method can transfer to other neural networks, rendering them equally ineffective at handling such adversarial inputs.

### III. METHODOLOGY

#### A. Framework of our model

In this paper, we propose a novel tunable neural network framework that integrates the high performance of neural networks with the inherent stability of diffusion equations, providing robustness against adversarial attacks by modulating the smoothness of outputs. Our model employs the unrolling algorithm to unfold the iterative process within a neural network, allowing end-to-end training with pairs of noisy images and their corresponding labels. The framework of our proposed model is illustrated in Figure 3.

The strength of our model lies in two aspects. First and foremost, no extra adversarial samples are needed to add to the training set compared to the adversarial training, which reduce the amount of calculation. Furthermore, the existence of diffusion equations enhances the robustness of our neural network, even effectively mitigates the effects of adversarial attacks. It is worth to mention that adjusting the only one parameter in our trained model can accommodate different degrees of disturbances from the ideal model (1). The details

and motivations behind each component of our model are provided below.

The powerful data-fitting ability of neural networks makes them very easy to overfit, which greatly affects the robustness of neural networks. The instability of neural networks makes them ineffective when the real data does not completely match the theoretical data. However, finding the most ineffective direction of neural networks and adding small perturbations is the core of adversarial attacks. Thus, the adversarial attacks can examine the robustness of a neural network. In addition, the networks with stronger denoising effects on simulated data tend to be more disturbed by adversarial samples, which can be observed from Figure 7.

To improve robustness while preserving the strong fitting capacity of neural network, we incorporate a diffusion equation  $\frac{\partial u}{\partial t} = \mathcal{H}(u, \nabla u)$  as a regularizer in the denoising network and unroll it to propose our framework. For  $k = 0, 1, \dots, K$ , formulating our model as

$$\begin{cases} z^{k+1} = \mathcal{D}_\theta(u^k) \\ u^{k+1} = z^{k+1} + \tau \mathcal{H}(u^{k+1}, \nabla u^{k+1}) \end{cases} \quad (7)$$

where  $u^0 = f$  is the noisy image,  $\mathcal{D}_\theta(\cdot)$  is a denoising neural network in (7), and (8) is the implicit scheme of diffusion equation with initial value  $z^{k+1}$  and time step  $\tau$ . In our model, the time step  $\tau$  can be adjusted at any stage, regardless of whether training has been completed. In some sense, the time step is one of hyperparameters in our network. The overall framework of the proposed method is shown in Figure 1.

Notably, our model can be regarded as a fitting-correction system. The denoising neural network unit  $\mathcal{D}_\theta(\cdot)$  exhibits strong fitting ability, while the diffusion regularity unit (8) enhances the smoothness of the denoised results, thereby preventing overfitting and improving stability. The core idea of our model is to smooth out the internal shocks caused by adversarial attacks in the network through the dissipation mechanism of the diffusion equation to improve the robustness.

The recursive architecture of our model is unrolled, as depicted in Figure 1, where the output of each iteration serves

as the input for the subsequent iteration. This unrolling framework induces a cumulative regularization effect throughout the network. Our model maintains the significant fitting capacity as a neural network, with its flexibility further augmented by the unrolling architecture, effectively modulating the smoothness of outputs. Under adversarial attacks, increasing the time step smooths the outputs, mitigating the additional noise introduced by such perturbations. Conversely, when the results are oversmoothed, reducing the time step decreases the smoothness and restores finer details, as illustrated in Figure 4.

### B. Diffusion regularity unit

The dissipative phenomenon of diffusion equations motivates their use as regularizer units in our model. The general diffusion equations can be written as

$$\frac{\partial u}{\partial t} = \text{div } D(u) \nabla u$$

where  $D(u)$  is the diffusion coefficient which controls the diffusion velocity and direction. The gradients in the distribution of  $u$  decrease, indicating a reduction in the disparities between high and low values of  $u$ . This reduction in gradients correlates with energy dissipation within the system. Importantly, the dissipative phenomenon occurs spontaneously and is independent of the noise distribution and its underlying mechanism. In other words, diffusion equations merely reduce the disparity between the maximum and minimum values in the input, irrespective of their cause.

Among the various linear and nonlinear diffusion equations, choosing the most simplest linear diffusion equation: Heat equation

$$\frac{\partial u}{\partial t} = \Delta u$$

as the regularizer can better highlight the effectiveness of our framework on increasing the network robustness by diffusion and reduce the computational cost. At that time, our model can be concretely described as

$$\begin{cases} z^{k+1} = \mathcal{D}_\Theta(u^k) \\ u^{k+1} = z^{k+1} + \tau \Delta u^{k+1} \end{cases} \quad (9)$$

$$(10)$$

It is widely accepted that nonlinear equations offer superior denoising and better edge preservation. However, in our case, the inherent nonlinearities of neural networks suffice to fully accomplish the denoising task. Furthermore, employing linear diffusion equations reduces computational complexity and simplifies theoretical analysis.

To explain more clearly the property of the dissipation mechanism of diffusion equation that insensitive to noise distribution, three different disturbances are shown in the Figure 2. The noisy signals are constructed by multiplying Gamma noise with  $L = 10$  to the original signal  $y = 1$  (red line) firstly to simulate the SAR images signal in one dimension, then adding Gaussian noise, Uniform noise, and Rayleigh Noise to 0-100, 100-200 and 200-300 respectively to simulate three different attacks. From Figure 2, the heat

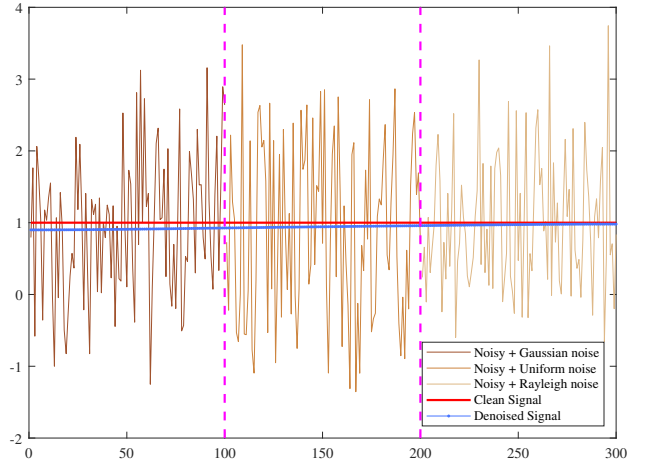


Fig. 2. The performance of heat equation to different noise

equation can restore these signals (blue line) no matter the causes are completely different.

The reason why we use implicit scheme in (10) to discrete heat equation is the unconditional stability of implicit scheme, which means that the time step can be changed arbitrary. The explicit scheme is the simplest to implement for discretizing the PDEs, but its stability is constrained by the Courant-Friedrichs-Lewy (CFL) condition. Large time step is necessary when resisting severe adversarial attack, which is the limitation of explicit scheme.

Consequently, from the theoretical perspective, the diffusion function unit in (10) accumulatively mitigates distortions inside the networks, which induced by adversarial attacks.

### C. Denoising neural network unit

Considering the diversity of methods for removing additive noise compared to multiplicative noise, transforming multiplicative noise into additive noise via a logarithmic transformation is a natural idea:

$$\log f = \log u + \log \eta$$

Here, the transformed observation  $\tilde{f} = \log f$  is no longer constrained to non-negative values. The SAR-CNN model [19] employs this strategy to process noisy images.

In principle, any denoising CNN can be selected as the denoising unit in our model, but, the number of layers of popular denoising networks is deep. Intuitively, deeper networks tend to yield superior denoising outcomes, but a shallow structure in each unit is sufficient to accomplish effective denoising under the recursive architecture. Additionally, Our goal is to construct a network that achieves excellent denoising results while increasing its robustness to prevent adversarial attack. Deeper layers induce more severe oscillations inside the network, necessitating larger time steps to ensure adequate regularization to counteract the oscillations induced by adversarial attacks. A deeper network will not only lead to a larger amount of computation, but also increase the error of the discrete scheme of the diffusion equation when the time step is increased. Thus, a shallow DnCNN denoising module [20] is employed as our denoising unit  $\mathcal{D}_\Theta(\cdot)$ .

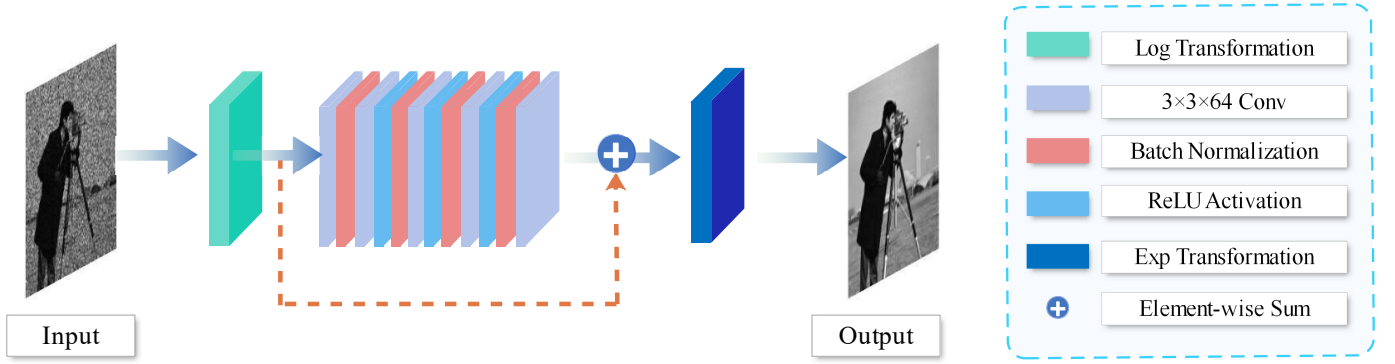


Fig. 3. The structure of denoising unit

For details, given a set of training samples  $f_i, y_i$ ,  $i = 1, \dots, N$ , where  $f_i$  and  $y_i$  represent noisy and clean images, respectively, the 5 layers DnCNN denoising module is used as the denoising unit  $\mathcal{D}_\Theta(\cdot)$ , which consists of five fully convolutional layers without any pooling. The filter sizes are  $3 \times 3 \times 64$ , and the input channel and the output channel are both set to 1. Since the DnCNN denoising module learns the noise distribution [20], a residual connection is established between the first and last layers. The network structure of denoising unit  $\mathcal{D}_\Theta(\cdot)$  is shown in Figure 3.

The entire network structure is obtained by arranging  $\mathcal{D}_\Theta(\cdot)$  and heat equations five times in sequence, which is denoted as  $\mathcal{W}_\Theta$ . Our network can be trained end-to-end, and the loss function [19] is

$$\mathcal{L}(\Theta) = \sum_{i=1}^N \mathbf{1}^\top \log \left( \cosh \left( \mathcal{W}_\Theta (\log f_i) + c - \log \frac{f_i}{y_i} \right) \right)$$

where  $c$  is the nonzero mean of log-speckle.

#### D. Theoretical analysis

There are numerous regularizer can be chose, such as TV regularizer, Tikhonov regularizer,  $p$ -laplacian and  $p(x)$ -laplacian regularizer. Reducing the computing complexity is only one side reason. Sufficient regularity is what we need, and the Theorem 1 [50] gives another reason why we choose heat equation as regularizer.

**Theorem 1.** Assume  $f \in C(\mathbb{R}^n) \cap L^\infty(\mathbb{R}^n)$ , then the solution of the following initial-value

$$\begin{cases} \frac{\partial u}{\partial t} = \Delta u \text{ in } \mathbb{R}^n \times (0, \infty) \\ u(x, 0) = f \text{ on } \mathbb{R}^n \times \{t = 0\} \end{cases}$$

is  $u(x, t) = \frac{1}{(4\pi t)^{n/2}} \int_{\mathbb{R}^n} e^{-\frac{|x-y|^2}{4t}} f(y) dy$ , and  $u \in C^\infty(\mathbb{R}^n \times (0, \infty))$ .

The proof of Theorem 1 can be found in [50]. When the noisy image  $f$  satisfies the condition in Theorem 1, the solution of heat equation is infinity smoothness, which provides sufficient regularity for our model. Moreover, the stability and convergence of our model can be given in Theorem 2 and Theorem 3 respectively.

**Lemma 1.** Suppose  $\Omega$  is a bounded open domain with Lipschitz boundary  $\partial\Omega$ , which contains the image domain. Besides, the heat equation satisfies the second boundary condition:  $\frac{\partial u}{\partial \vec{n}} = 0$  on  $\partial\Omega$ , where  $\vec{n}$  is the outer normal vector of  $\Omega$ . Assume the neural network  $\mathcal{D}_\Theta(\cdot)$  is non-expandable:

$$|\mathcal{D}_\Theta(u_1) - \mathcal{D}_\Theta(u_2)| \leq \varepsilon |u_1 - u_2|$$

for any  $0 < \varepsilon \leq 1$  and its weak derivative piecewise continuous with  $|\nabla \mathcal{D}_\Theta(\cdot)| \leq 1$ . Then, for the sequence  $\{u^k\}_{k=0}^K$  generated by our algorithm satisfies the following inequality

$$\sum_{k=0}^K \|u^{k+1} - \mathcal{D}_\Theta(u^k)\|_{L^2(\Omega)}^2 \leq \frac{\tau}{2} \|u^0\|_{L^2(\Omega)}^2$$

From Lemma 1, the stability analysis or the continuous dependence of solutions on initial values can be given.

**Theorem 2 (Stability).** If the neural network  $\mathcal{D}_\Theta(\cdot)$  satisfies the conditions in Lemma 1, our algorithm is stable.

Theorem 2 implies the continuous dependency of the solutions  $u^{k+1}$  to initial value  $u^0$  for each  $k > 0$ .

**Theorem 3 (Convergence).** If the neural network  $\mathcal{D}_\Theta(\cdot)$  satisfies the conditions in Lemma 1 and the  $\varepsilon < 1$ , then the sequence  $\{u^k\}_{k=0}^K$  generated by our algorithm is globally convergent.

#### E. Numerical scheme of diffusion unit

The unrolling scheme ensures an even distribution of diffusion equation units across the network, cumulatively enhancing the regularization of the entire model. Adjusting the time step  $\tau$  modulates the smoothness of the denoised image post-training.

First, we assume that the periodic boundary condition is imposed on the heat equation. The shifting operators are denoted by  $\mathcal{S}_x^\pm u(i, j) = u(i \pm 1, j)$  and  $\mathcal{S}_y^\pm u(i, j) = u(i, j \pm 1)$ . Consider the implicit scheme for the heat equation in two dimensions

$$u^{k+1} = u^k + \tau (D_x^- D_x^+ u^{k+1} + D_y^- D_y^+ u^{k+1}) \quad (11)$$

where the  $D_x^\pm$  and  $D_y^\pm$  are the forward (backward) operators on the direction  $x$  and  $y$  respectively. Thus, they can be

presented as  $D_x^- D_x^+ = \mathcal{S}_x^- - 2\mathcal{I} + \mathcal{S}_x^+$  and  $D_y^- D_y^+ = \mathcal{S}_y^- - 2\mathcal{I} + \mathcal{S}_y^+$ , where  $\mathcal{I}$  is the identity operator. For discrete frequencies  $x_i$  and  $y_j$ , we have [51]:

$$\begin{aligned}\mathcal{F}\mathcal{S}_x^\pm u(x_i, y_j) &= e^{\pm\sqrt{-1}z_i} \mathcal{F}u(x_i, y_j) \\ \mathcal{F}\mathcal{S}_y^\pm u(x_i, y_j) &= e^{\pm\sqrt{-1}z_j} \mathcal{F}u(x_i, y_j)\end{aligned}$$

where

$$z_i = \frac{2\pi}{N_1} x_i, i = 1, 2, \dots, N_1 \quad z_j = \frac{2\pi}{N_2} y_j, j = 1, 2, \dots, N_2$$

Thus, the (11) can be rewritten as

$$(-2\tau(\cos(z_i) + \cos(z_j)) - 2) + 1) \mathcal{F}u^{k+1}(x_i, y_j) = \mathcal{F}u^k(x_i, y_j) \quad (12)$$

The discrete inverse Fourier transformation  $\mathcal{F}^{-1}$  can be directly applied to the solution of (12) to obtain the updated  $u^{k+1}$ .

The whole algorithm of our model is given in Algorithm 1.

---

#### Algorithm 1 algorithm of our model

---

##### TRAIN

Input: noisy image  $f$ , clean image  $y$

Initialization:

- (1) Set parameters:  $K$ ,  $\tau$  and the parameters in  $\mathcal{D}_\Theta(\cdot)$
- (2) Initialize  $u^0 = f$
- (3) Acquire input size  $N_1$  and  $N_2$

for  $k$  from 1 to  $K$

$$z^{k+1} \leftarrow \mathcal{D}_\Theta(u^k)$$

for  $x_i$  from 1 to  $N_1$  and  $y_j$  from 1 to  $N_2$ :

$$u^{k+1}(x_i, y_j) \leftarrow \mathcal{F}^{-1} \left( \frac{\mathcal{F}z^k(x_i, y_j)}{-2\tau(\cos(\frac{2\pi}{N_1}x_i) + \cos(\frac{2\pi}{N_2}y_j) - 2) + 1} \right)$$

return  $u^{k+1}$

$loss \leftarrow \mathcal{L}(u^{k+1}, y)$

$loss.back()$  to update the parameters in our model

##### PREDICT

Input: noisy image  $f$

Initialization:

- (1) Set a proper  $\tau$
- (2) Initialize  $u^0 = f$
- (3) Acquire input size  $N_1$  and  $N_2$

for  $k$  from 1 to  $K$

$$z^{k+1} \leftarrow \mathcal{D}_\Theta(u^k)$$

for  $x_i$  from 1 to  $N_1$  and  $y_j$  from 1 to  $N_2$ :

$$u^{k+1}(x_i, y_j) \leftarrow \mathcal{F}^{-1} \left( \frac{\mathcal{F}z^k(x_i, y_j)}{-2\tau(\cos(\frac{2\pi}{N_1}x_i) + \cos(\frac{2\pi}{N_2}y_j) - 2) + 1} \right)$$

return  $u^{k+1}$

---

#### F. Controllable smoothness

To visually assess the effect of the time step on smoothness, an experiment is illustrated in Figure 4. After training the network with a time step of  $\tau = 0.1$ , and the unrolling depth  $K = 5$ , an adversarial sample generated by SAR-CNN was selected as input. Increasing the time step from 0.06 to 0.20 leads to a significant increase in smoothness. As shown in Figure 4, smaller time steps such as  $\tau = 0.08$  and  $\tau = 0.1$

retain more details but exhibit lower denoising effects. Larger time steps result in greater smoothness, with many details being smoothed out. This experiment verifies the feasibility of our strategy of controlling smoothness by controlling the time step.

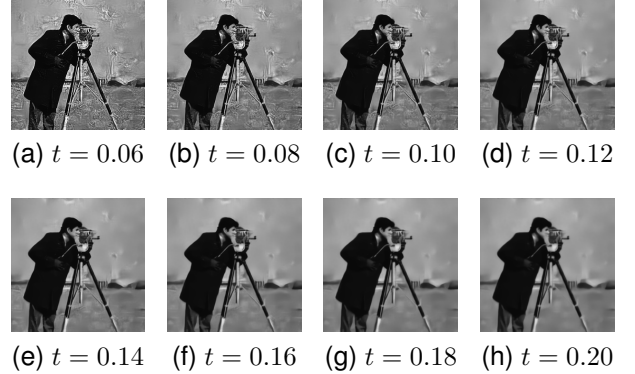


Fig. 4. The results of our model with variance of  $t$  for Cameraman

In summary, we propose a tunable cumulative regularization network composed of a shallow denoising unit and a diffusion equation regularization unit. The unrolling structure allows the shallow denoising unit to produce satisfactory results, while the diffusion equation unit contributes to the cumulative regularization of the model. The linear diffusion equation in the regularization unit is sufficient, as the denoising units introduce the necessary nonlinearities. We demonstrate the effectiveness of our model from the principle and experimental results, and further provide the stability and convergence analysis of our model.

## IV. EXPERIMENT

### A. Data

We randomly selected 400 images for training and 68 images for validation from the BSR-BSDS500 dataset. Noisy images were generated by adding multiplicative Gamma noise to both the training and validation sets after converting the color images to grayscale, with a noise level of  $L = 1, 4, 10$ .

The test data comprises two types: simulated images and real SAR images. For the simulated images, multiplicative Gamma noise with  $L = 1, 4, 10$  was added to three publicly available datasets: Set12 [52], McMaster [53], FloodNet Dataset [54] and RESISC45 [55]. It must be pointed out that 12 images and 14 images are picked randomly in the FloodNet Dataset and RESISC45 as the representatives of their data set, because the data volume of the complete data sets is huge. In addition, we selected the first ten images from the Set12 dataset as the test images, following the procedure outlined in [19]. To prevent the emergence of idiosyncratic samples, noise was randomly added to each image 10 times, resulting in each clean test image corresponding to 10 noisy images. Three real SAR images were used for evaluation of our method, as shown in Figure 5. For simplicity, these images are denoted as SAR1

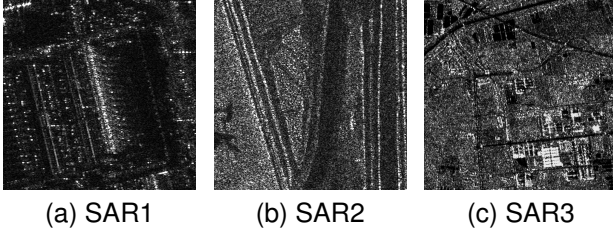


Fig. 5. Real SAR images

( $512 \times 512$ ), SAR2 ( $512 \times 512$ ), and SAR3 ( $512 \times 512$ ), which are selected from ICEYE <sup>1</sup> and Gaofen-3 satellite <sup>2</sup>.

### B. Experimental Setup and training

In this study, our network utilized the Adam optimizer, with a minibatch size of 128 patches, and adopted the batch normalization technique described in [56]. The model was trained for 50 epochs, with learning rates 0.001 for the first 30 epochs and reduced to 0.0001 for the subsequent 20 epochs. Following data augmentation, the training set was composed of  $2000 \times 128$  patches, with each patch including  $40 \times 40$  pixels.

During training, the time step in the diffusion equation unit and the unrolling depth were set to  $\tau = 0.1$  and  $K = 5$  respectively. After training, the time step can be adjusted freely, while the other network parameters remain fixed. Throughout the training and testing phases, all code was implemented by PyTorch framework.

1) *Evaluation Index*: This paper adopts two distinct evaluation strategies for simulated and real SAR images.

For simulated images, evaluation metrics include the peak signal-to-noise ratio (PSNR) and the structural similarity image measurement (SSIM). Here, the clean image and denoised image are denoted as  $y$  and  $\hat{y}$  respectively.

$$\text{PSNR} = 10 \log_{10} \frac{IJ255 * 255}{\|\hat{y} - y\|_{L^2}^2}$$

$$\text{SSIM} = \frac{(2\mu_y\mu_{\hat{y}} + c_1)(2\sigma_{\hat{y}y} + c_2)}{(\mu_{\hat{y}}^2 + \mu_y^2 + c_1)(\sigma_{\hat{y}}^2 + \sigma_y^2 + c_2)}$$

where  $I$  and  $J$  are height and width of the image respectively;  $\mu_{\hat{y}}$  and  $\mu_y$  represent the mean of  $\hat{y}$  and  $y$ ;  $\sigma_{\hat{y}}^2$  and  $\sigma_y^2$  represent the variance of  $\hat{y}$  and  $y$ ;  $\sigma_{\hat{y}y}$  is the covariance between  $\hat{y}$  and  $y$ ;  $c_1$  and  $c_2$  are constants. Higher PSNR values indicate that the denoised image more closely resembles the original clean image. Additionally, SSIM effectively assesses edge preservation, where higher values correspond to greater edge recovery ability.

For real SAR images, in the absence of ground-truth, the evaluation of denoising cleanliness is based on the equivalent number of looks (ENL)

$$\text{ENL} = \frac{\bar{\hat{y}}^2}{\sigma_{\hat{y}}^2}$$

where  $\bar{\hat{y}}^2$  and  $\sigma_{\hat{y}}^2$  are the mean and the variance of the restored image respectively. The edge preservation degree is determined by the ratio of the standard deviation  $\sigma_{\hat{y}}^2$  to the mean intensity  $\mu_{\hat{y}}$  (Cx) and the ratio of average (EPD-ROA) for horizontal direction (HD) and vertical direction (VD)

$$\text{Cx} = \frac{\sigma_{\hat{y}}}{\mu_{\hat{y}}}, \quad \text{EPD-ROA} = \frac{\sum_{i=1}^m |I_{D1}(i)/I_{D2}(i)|}{\sum_{i=1}^m |I_{O1}(i)/I_{O2}(i)|}$$

where  $I_{D1}(i)$  and  $I_{D2}(i)$  are the adjacent pixels on the horizontal and vertical direction of denoised image.  $I_{O1}(i)$  and  $I_{O2}(i)$  are the adjacent pixels on the horizontal and vertical direction of noisy image. In a homogeneous area, large (small) coefficient of ENL (Cx) represents great speckle removal performance. The closer of RPD-ROA value to 1, the more details are protected.

2) *Comparison Method*: The experimental procedure is divided into three distinct phases: simulated image experiments, adversarial image experiments, and real SAR image tests. We compare the proposed model against one traditional method, MuLoG-BM3D [57], and four state-of-the-art neural network (NN)-based methods: SAR-CNN [19], AGSDNet [58], SAR-RDCP [26], and TB-SAR [59]. Among the NN-based methods, SAR-CNN represents the earliest application of deep learning for multiplicative noise removal. AGSDNet integrates image gradient information, channel attention, and spatial attention mechanisms into the network, resulting in enhanced performance. SAR-RDCP substitutes the traditional regularizer with a neural network in a variational model and unrolls its algorithm into the network, effectively enhancing despeckling. In contrast to the above CNN-based methods, TB-SAR is a denoising model specifically designed under the transformer framework.

### C. Results on simulated images

In denoising experiments with simulated SAR images, both visual evaluation and quantitative comparison are essential. In this experiment, all the test images are selected from Set12, McMaster, FloodNet Dataset and RESISC45, and corrupted by multiplicative Gamma noise with noise level  $L = 1, 4, 10$ .

Tables I present the average PSNR and SSIM for each test image, with the best values highlighted in bold. It is evident that the traditional method MuLoG-BM3D exhibits the lowest PSNR and SSIM in comparison to NN-based methods, further demonstrating the significant advantages of neural networks. As shown in Tables I, our model provides superior detail preservation (SSIM) and enhanced despeckling capability (PSNR) compared to other methods, regardless of the noise level. SARCNN and AGSDNet exhibit comparable performance to our model when the noisy level  $L = 4$  and  $10$ , but AGSDNet shows better denoising results when  $L = 1$ . For the FloodNet dataset, the BM3D method shows higher SSIM when  $L = 4$  and  $10$ , only slightly higher than our method.

From a visual perspective, the denoising capability of a model is generally performed on smooth backgrounds, preserve edges, and retain textures. To address these three aspects, we select representative images from the test sets to illustrate the key characteristics of our model. The all images are

<sup>1</sup><https://www.iceye.com/downloads/datasets>

<sup>2</sup><https://github.com/AmberHen/WHU-OPT-SAR-dataset>

TABLE I  
THE COMPARISON OF PSNR AND SSIM ON SIMULATE IMAGES

| Dataset  | Looks | MuLoG-BM3D |             | SAR-CNN |             | AGSDNet |      | SAR-RDCP |      | TB-SAR |      | Ours         |             |
|----------|-------|------------|-------------|---------|-------------|---------|------|----------|------|--------|------|--------------|-------------|
|          |       | PSNR       | SSIM        | PSNR    | SSIM        | PSNR    | SSIM | PSNR     | SSIM | PSNR   | SSIM | PSNR         | SSIM        |
| Set12    | L=1   | 21.52      | 0.75        | 24.67   | 0.71        | 25.64   | 0.74 | 23.36    | 0.68 | 24.64  | 0.71 | <b>25.78</b> | <b>0.77</b> |
|          | L=4   | 26.65      | 0.82        | 29.04   | <b>0.85</b> | 28.72   | 0.83 | 28.44    | 0.82 | 27.03  | 0.77 | <b>29.17</b> | <b>0.85</b> |
|          | L=10  | 29.02      | 0.87        | 30.57   | 0.85        | 30.93   | 0.87 | 30.57    | 0.87 | 28.43  | 0.81 | <b>31.15</b> | <b>0.89</b> |
| McMaster | L=1   | 22.60      | 0.71        | 25.59   | 0.76        | 26.16   | 0.77 | 22.12    | 0.70 | 25.12  | 0.72 | <b>26.33</b> | <b>0.80</b> |
|          | L=4   | 26.77      | 0.80        | 29.72   | 0.88        | 29.40   | 0.87 | 29.16    | 0.86 | 27.36  | 0.80 | <b>29.84</b> | <b>0.89</b> |
|          | L=10  | 29.11      | 0.86        | 31.64   | 0.90        | 31.79   | 0.91 | 31.50    | 0.91 | 28.85  | 0.83 | <b>32.25</b> | <b>0.93</b> |
| FloodNet | L=1   | 22.56      | 0.71        | 25.21   | 0.61        | 27.05   | 0.66 | 22.86    | 0.61 | 26.46  | 0.63 | <b>27.14</b> | <b>0.69</b> |
|          | L=4   | 27.45      | <b>0.79</b> | 29.49   | 0.77        | 29.41   | 0.75 | 29.28    | 0.75 | 28.07  | 0.69 | <b>29.66</b> | 0.78        |
|          | L=10  | 29.16      | <b>0.84</b> | 30.79   | 0.80        | 31.22   | 0.81 | 31.12    | 0.81 | 29.15  | 0.73 | <b>31.47</b> | 0.83        |
| NWPU     | L=1   | 21.26      | 0.64        | 23.70   | 0.67        | 24.41   | 0.70 | 21.28    | 0.65 | 23.59  | 0.65 | <b>24.57</b> | <b>0.72</b> |
|          | L=4   | 25.41      | 0.74        | 27.61   | <b>0.83</b> | 27.35   | 0.81 | 27.09    | 0.81 | 25.82  | 0.74 | <b>27.69</b> | <b>0.83</b> |
|          | L=10  | 27.33      | 0.79        | 29.36   | 0.87        | 29.52   | 0.87 | 29.29    | 0.87 | 27.24  | 0.78 | <b>29.84</b> | <b>0.88</b> |

selected under the noise level  $L = 1$ , which is the worst situation in real life to test the capability of models to cope with the most complex environments.

The first two images selected in Figure 6 share two common characteristics: uniform grayscale in large areas and high-contrast edges. In the restoration results of these two images, all methods demonstrate excellent preservation of strong (coarse) edges in the restored images. Furthermore, our model, AGSDNet, and MuLoG-BM3D effectively remove background noise, with our model and AGSDNet producing sharper edges in the restored results.

The third and fourth images in Figure 6 contain rich weak edge informations, such as the camera tripods in the third image, and triangular building on the roof in the fourth image, these are overly smoothed by the MuLoG-BM3D, SAR-RDCP, and TBSAR methods. Additionally, for the camera tripods in the third image, our model and SAR-CNN produce similar results, outperforming AGSDNet and other methods.

The restoration of texture is shown in the last two images in Figure 6. Our model achieves similar results to SAR-CNN on the last image, outperforming the other compared models. Our model, SAR-CNN and AGSDNet have similar restoration results on the pattern on the roof of church.

In summary, our model demonstrates superior performance on simulated images compared to the other models both on evaluation index and visual effect.

#### D. Results on adversarial samples

Due to the instability of neural networks, their performance on real data often falls short compared to their performance on simulated datasets. In this section, adversarial attacks are employed to simulate severe perturbations between real-world and simulated data, serving as a benchmark to evaluate the robustness of the proposed network.

As mentioned earlier, the adversarial samples generated by denoising-PGD exhibit strong transferability across NN-based methods, allowing a single adversarial sample to effectively attack all such models [33]. In subsection III-B, the principle that our model can counter such adversarial attacks had been explained, and in this section, we verify its effectiveness through experimental evidence. In this experiment, the images in Set12 are selected as the attack target, and all adversarial samples were generated from a 10-layer SAR-CNN.

Table II lists the PSNR values of all the methods on the adversarial images. Because of the adding of new adversarial noise to the original noisy image, the decline of evaluation index is inevitable. From quantitative index, our model has similar performance with AGSDNet, but a little better than AGSDNet. Furthermore, the PSNR values of our model and AGSDNet are much better than the other compared models.

The primary advantages of our model are reflected in its superior visual performance. Our model effectively suppresses high-frequency oscillations within the neural network, thereby enhancing restoration quality. Figure 7 illustrates the visual performance of various NN-based models on adversarial samples. The first and second columns depict the adversarial samples and its differences with the original noisy images, respectively. The third to sixth columns show the results generated by different NN-based approaches.

As shown in Figure 7, all restored images from the compared methods exhibit oscillations in the background and main objects, which should not occur. The results produced by SAR-CNN and AGSDNet display high-frequency oscillations in the background and detailed regions, negatively impacting object recognition. The results generated by TB-SAR have blurred edges, which reduces the overall restoration quality. Due to the cumulative regularization, the images restored by our model exhibit superior denoising effects and sharper edges compared to those restored by other models. Our model removes unnecessary high-frequency oscillations in edges and backgrounds while preserving image details.

The adversarial experiments demonstrate the stability of our model, providing strong evidence for its underlying principles and theoretical framework. Consequently, our model is well-suited for the complex real-world scenarios.

TABLE II  
THE PSNR ON THE ADVERSARIAL SAMPLES GENERATED BY SET12

| Dataset | SAR-CNN | AGSDNet | SAR-RDCP | TB-SAR | Ours  |
|---------|---------|---------|----------|--------|-------|
| Set12   | 23.73   | 24.15   | 22.31    | 23.85  | 24.19 |

#### E. Results on real SAR images

This section presents the performance comparison of all models on real SAR images. Three SAR images representing



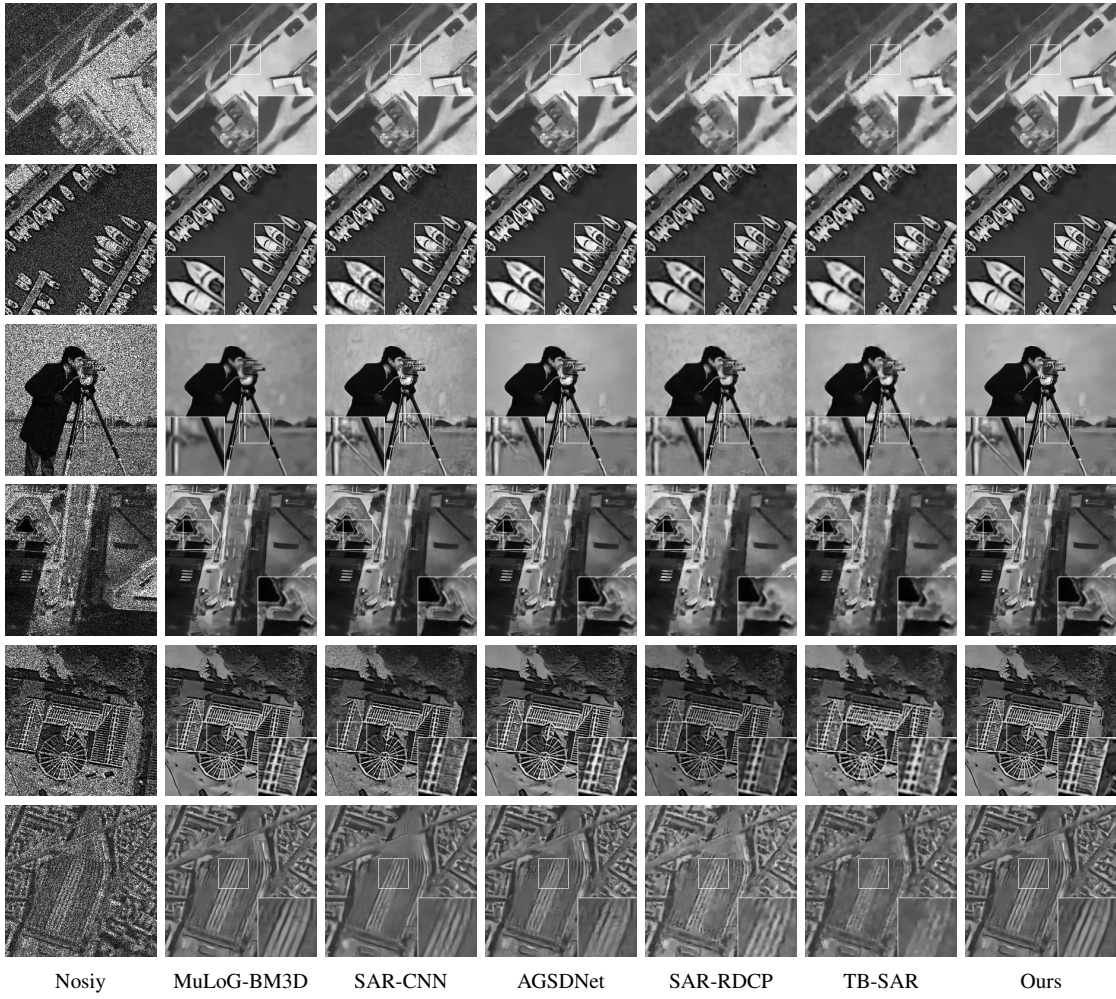


Fig. 6. Restoration results for images with enlarged areas of the same grayscale with noise level  $L = 1$

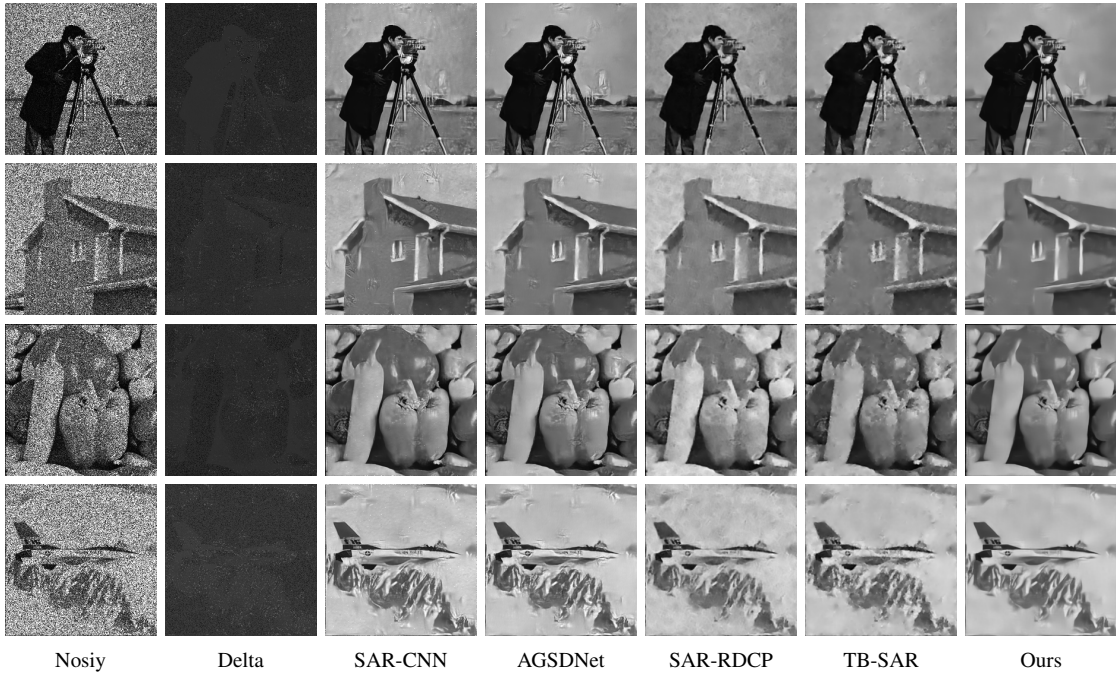


Fig. 7. Restoration results for adversarial images based on noisy images with  $L = 1$

distinct scenarios are shown in Figure 5.

Figure 8 compares the restoration results of our method with other competing models. We employ three distinct time steps,  $\tau = 0.020, 0.100, \text{ and } 0.180$ , to highlight the adaptability of our model in controlling result smoothness, as illustrated in the final three images of Figure 8.

In Figure 8, the results given by AGSDNet and SAR-RDCP are not satisfactory, because the results from them retain significant noise. Moreover, while SAR-CNN is more effective at removing noise compared to the above two models, it introduces white spots that significantly affect both the visual quality and the calculation of ENL and Cx. Mulog-BM3D, TB-SAR, and our model yield acceptable results in terms of balancing noise removal and detail preservation.

Compared to other approaches, our model achieves an optimal trade-off between noise removal and detail preservation, owing to its ability to adjust smoothness adaptively. Smaller time steps prioritize detail preservation, whereas larger time steps enhance noise reduction, as evidenced by the final three images in Figure 8. Unlike traditional neural networks that the outputs are fixed, the flexibility of our model significantly enhances the controllability of the results.

Among all methods, our model demonstrates superior noise removal at  $\tau \geq 0.1$  and performs comparably to Mulog-BM3D in detail preservation at  $\tau = 0.02$ . For example, in the bottom-right region of SAR3, Mulog-BM3D restores a white square with black lines. Our model effectively reconstructs the primary lines in this region, whereas TB-SAR overly smooths finer details. While Mulog-BM3D excels at detail preservation, its outputs exhibit undesirable ripples, notably on the left side of SAR2.

Table III summarizes the ENL, Cx and RPD-ROA metrics for the results of all methods on the three SAR images. In Table III, the best values are highlighted in bold. It is important to note that the images restored by SAR-CNN contain numerous unintended white specks, significantly distorting its performance metrics. As a result, the calculated ENL and Cx metrics for SAR-CNN are unreliable and provide limited informative value. Moreover, similar results were obtained by both TB-SAR and our method in terms of the denoising metrics ENL and Cx, which reflects the cleanliness of denoising, and also corresponds to the visual results in Figure 8. The SAR-RDCP model achieves the highest EPD-ROA, indicating superior detail retention, followed by our model, which secures the second-highest rank. The accumulative regularization in our model ensures smooth outputs, which explains its slightly lower EPD-ROA performance compared to SAR-RDCP.

Considering both visual quality and evaluation metrics, our model effectively removes noise from real SAR images while maintaining excellent detail preservation. Most importantly, our model exhibits high flexibility compared to other traditional neural networks.

## V. CONCLUSION

In this study, we propose a novel tunable multiplicative denoising network with cumulative regularization, designed to mitigate adversarial attacks. Drawing inspiration from the

TABLE III  
THE COMPARISON OF ENL AND Cx ON REAL SAR IMAGES

| Images               | Methods              | ENL          | Cx     | EPD-ROA      |              |
|----------------------|----------------------|--------------|--------|--------------|--------------|
|                      |                      |              |        | HD           | VD           |
| SAR1                 | Mulog-BM3D           | 1.618        | 0.786  | 0.571        | 0.579        |
|                      | SAR-CNN              | 0.001        | 29.760 | 0.640        | 0.646        |
|                      | AGSDNet              | 1.282        | 0.883  | 0.595        | 0.621        |
|                      | SAR-RDCP             | 1.524        | 0.809  | <b>0.688</b> | <b>0.782</b> |
|                      | TB-SAR               | 1.859        | 0.733  | 0.569        | 0.574        |
|                      | Ours- $\tau = 0.020$ | 1.250        | 0.894  | 0.602        | 0.664        |
|                      | Ours- $\tau = 0.100$ | 1.873        | 0.731  | 0.568        | 0.575        |
| Ours- $\tau = 0.180$ | <b>2.281</b>         | <b>0.662</b> | 0.564  | 0.565        |              |
| SAR2                 | Mulog-BM3D           | 4.545        | 0.469  | 0.604        | 0.594        |
|                      | SAR-CNN              | 0.001        | 63.351 | 0.720        | 0.729        |
|                      | AGSDNet              | 3.795        | 0.513  | 0.624        | 0.620        |
|                      | SAR-RDCP             | 3.112        | 0.567  | <b>0.740</b> | <b>0.751</b> |
|                      | TB-SAR               | 6.436        | 0.394  | 0.595        | 0.591        |
|                      | Ours- $\tau = 0.020$ | 4.805        | 0.456  | 0.618        | 0.602        |
|                      | Ours- $\tau = 0.100$ | 6.467        | 0.393  | 0.598        | 0.590        |
| Ours- $\tau = 0.180$ | <b>7.277</b>         | <b>0.371</b> | 0.595  | 0.589        |              |
| SAR3                 | Mulog-BM3D           | 2.889        | 0.588  | 0.408        | 0.400        |
|                      | SAR-CNN              | 0.143        | 2.640  | 0.539        | 0.532        |
|                      | AGSDNet              | 2.267        | 0.664  | 0.529        | 0.481        |
|                      | SAR-RDCP             | 2.844        | 0.593  | <b>0.899</b> | 0.697        |
|                      | TB-SAR               | 3.665        | 0.522  | 0.400        | 0.422        |
|                      | Ours- $\tau = 0.020$ | 2.296        | 0.660  | 0.845        | <b>0.720</b> |
|                      | Ours- $\tau = 0.100$ | 3.416        | 0.541  | 0.446        | 0.432        |
| Ours- $\tau = 0.180$ | <b>3.899</b>         | <b>0.506</b> | 0.395  | 0.393        |              |

dissipative phenomenon of diffusion equations, which enables denoising independent of noise distribution, we incorporate a linear heat equation as a unit within the network to impose regularization. Leveraging the unrolling technique, cumulative regularization is achieved by unfolding our algorithm into a neural network. The flexibility of our deep neural network is significantly enhanced compared to traditional networks, enabling the adjustment of smoothness levels by tuning the time step  $\tau$  after end-to-end training.

After proving the stability and convergence of our model, five other mainstream methods are selected for comparative experiment on simulated data, adversarial data, and real-world data. The superior denoising capability of our model, particularly in preserving background, weak edges, and texture, is shown in experiments. At the same time, the robustness of our neural network against adversarial attacks is also illustrated experimentally. Finally, our model performs well in visual effects on real SAR images.

## ACKNOWLEDGMENTS

The authors acknowledge support from DESY (Hamburg, Germany), a member of the Helmholtz Association HGF. Yi Ran acknowledges the support of the China Scholarship Council program.

## APPENDIX PROOF OF THE THEOREMS

*Proof of Lemma 1.* The recursive algorithm of ours can be rewritten as

$$u^{k+1} = \mathcal{D}_\Theta(u^k) + \tau \Delta u^{k+1} \quad (13)$$

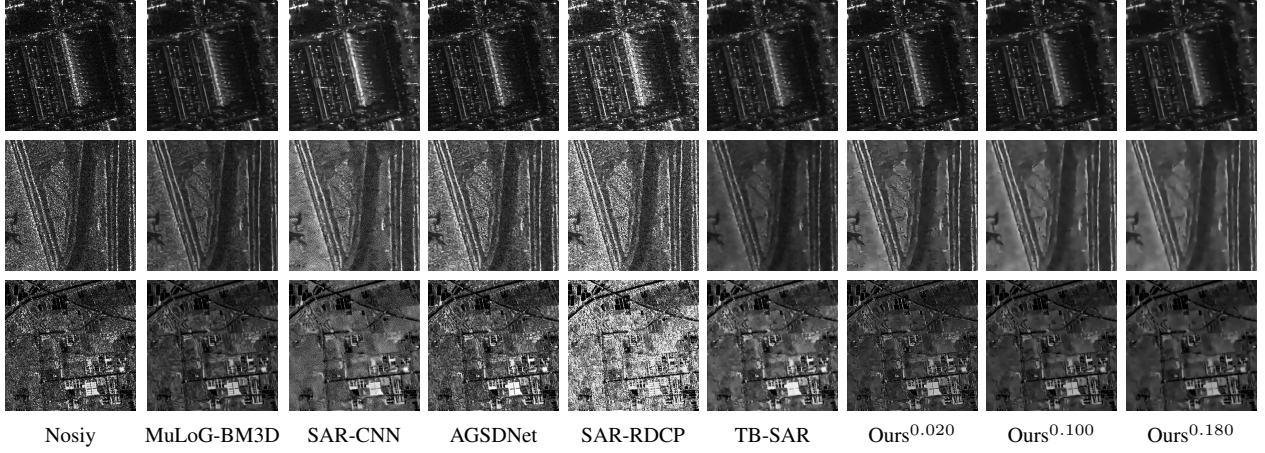


Fig. 8. Restoration results for images with texture with noise level  $L = 1$

from  $k$  step to  $k + 1$  step. Multiply the  $u^{k+1} - \mathcal{D}_\Theta(u^k)$  on the both hands and integrate on  $\Omega$ , we have

$$\|u^{k+1} - \mathcal{D}_\Theta(u^k)\|_{L^2(\Omega)}^2 = \int_{\Omega} \tau(u^{k+1} - \mathcal{D}_\Theta(u^k))\Delta u^{k+1} dx$$

According to the integrate by parts formula and Cauchy inequality, it follows that

$$\begin{aligned} & \|u^{k+1} - \mathcal{D}_\Theta(u^k)\|_{L^2(\Omega)}^2 + \tau \int_{\Omega} |\nabla u^{k+1}|^2 dx \\ & \leq \tau \int_{\Omega} |\nabla \mathcal{D}_\Theta(u^k) \nabla u^{k+1}| dx \\ & \leq \frac{\tau}{2} \int_{\Omega} |\nabla \mathcal{D}_\Theta(u^k)|^2 dx + \frac{\tau}{2} \int_{\Omega} |\nabla u^{k+1}|^2 dx \end{aligned} \quad (14)$$

Sum both sides of (14) for  $k$ , under the condition  $|\nabla \mathcal{D}_\Theta(\cdot)| \leq 1$ , we have

$$\sum_{k=0}^K \|u^{k+1} - \mathcal{D}_\Theta(u^k)\|_{L^2(\Omega)}^2 \leq \frac{\tau}{2} \|u^0\|_{L^2(\Omega)}^2 \quad (15)$$

□

*Proof of Theorem 2.* For the iterating step  $k$  to  $k+1$ , multiply  $u^{k+1}$  on the both sides of (13) and integrate on  $\Omega$ , we have

$$\|u^{k+1}\|_{L^2(\Omega)}^2 = \int_{\Omega} u^{k+1}(\mathcal{D}_\Theta(u^k) + \tau \Delta u^{k+1}) dx$$

By the non-expandable of  $\mathcal{D}_\Theta(\cdot)$  and integrate by parts, we have

$$\begin{aligned} & \|u^{k+1}\|_{L^2(\Omega)}^2 + \tau \int_{\Omega} |\nabla u^{k+1}|^2 dx \\ & = \int_{\Omega} u^{k+1} \mathcal{D}_\Theta(u^k) dx \\ & \leq \frac{1}{2} \int_{\Omega} |u^{k+1}|^2 dx + \frac{1}{2} \int_{\Omega} |\mathcal{D}_\Theta(u^k)|^2 dx \end{aligned}$$

which implies that

$$\|u^{k+1}\|_{L^2(\Omega)} \leq \varepsilon^{k+1} \|u^0\|_{L^2(\Omega)} \quad (16)$$

□

*Proof of Theorem 3.* According to the minkowski inequality, conditions of  $\mathcal{D}_\Theta(\cdot)$  and the inequality (15) and (16), we have

$$\begin{aligned} & \|u^{k+1} - u^k\|_{L^2(\Omega)} \\ & \leq \|u^{k+1} - \mathcal{D}_\Theta(u^k)\|_{L^2(\Omega)} + \|\mathcal{D}_\Theta(u^k)\|_{L^2(\Omega)} \\ & \leq \left(\sqrt{\frac{\tau}{2}} + \varepsilon^k\right) \|u^0\|_{L^2(\Omega)} \end{aligned}$$

which means that  $\|u^{k+1} - u^k\|_{L^2(\Omega)} \rightarrow 0$  as  $k \rightarrow \infty$  and  $\tau \rightarrow 0$ . □

## REFERENCES

- [1] G. Krieger, I. Hajnsek, K. P. Papathanassiou, M. Younis, and A. Moreira, "Interferometric synthetic aperture radar (sar) missions employing formation flying," *Proceedings of the IEEE*, vol. 98, no. 5, pp. 816–843, 2010.
- [2] Q. Zhang, Q. Yuan, J. Li, Z. Yang, and X. Ma, "Learning a dilated residual network for sar image despeckling," *Remote Sensing*, vol. 10, no. 2, p. 196, 2018.
- [3] X. Ma, H. Shen, J. Yang, L. Zhang, and P. Li, "Polarimetric-spatial classification of sar images based on the fusion of multiple classifiers," *IEEE Journal of Selected Topics in Applied Earth Observations and Remote Sensing*, vol. 7, no. 3, pp. 961–971, 2013.
- [4] J. W. Goodman, "Some fundamental properties of speckle," *JOSA*, vol. 66, no. 11, pp. 1145–1150, 1976.
- [5] —, "Statistical properties of laser speckle patterns," in *Laser speckle and related phenomena*. Springer, 1975, pp. 9–75.
- [6] J.-S. Lee, "Digital image enhancement and noise filtering by use of local statistics," *IEEE transactions on pattern analysis and machine intelligence*, no. 2, pp. 165–168, 1980.
- [7] D. T. Kuan, A. A. Sawchuk, T. C. Strand, and P. Chavel, "Adaptive noise smoothing filter for images with signal-dependent noise," *IEEE transactions on pattern analysis and machine intelligence*, no. 2, pp. 165–177, 1985.
- [8] V. S. Frost, J. A. Stiles, K. S. Shanmugan, and J. C. Holtzman, "A model for radar images and its application to adaptive digital filtering of multiplicative noise," *IEEE Transactions on pattern analysis and machine intelligence*, no. 2, pp. 157–166, 1982.
- [9] A. Lopes, E. Nezry, R. Touzi, and H. Laur, "Maximum a posteriori speckle filtering and first order texture models in sar images," in *10th annual international symposium on geoscience and remote sensing*. Ieee, 1990, pp. 2409–2412.
- [10] A. Buades, B. Coll, and J.-M. Morel, "A review of image denoising algorithms, with a new one," *Multiscale modeling & simulation*, vol. 4, no. 2, pp. 490–530, 2005.
- [11] G. Aubert and J.-F. Aujol, "A variational approach to removing multiplicative noise," *SIAM journal on applied mathematics*, vol. 68, no. 4, pp. 925–946, 2008.
- [12] J. Shi and S. Osher, "A nonlinear inverse scale space method for a convex multiplicative noise model," *SIAM Journal on imaging sciences*, vol. 1, no. 3, pp. 294–321, 2008.

- [13] G. Dong, Z. Guo, B. Wu *et al.*, “A convex adaptive total variation model based on the gray level indicator for multiplicative noise removal,” in *Abstract and Applied Analysis*, vol. 2013. Hindawi, 2013.
- [14] Z. Zhou, Z. Guo, G. Dong, J. Sun, D. Zhang, and B. Wu, “A doubly degenerate diffusion model based on the gray level indicator for multiplicative noise removal,” *IEEE Transactions on Image Processing*, vol. 24, no. 1, pp. 249–260, 2014.
- [15] A. Laghrib and L. Afraïtes, “Image denoising based on a variable spatially exponent pde,” *Applied and Computational Harmonic Analysis*, vol. 68, p. 101608, 2024.
- [16] W. Yao, Z. Guo, J. Sun, B. Wu, and H. Gao, “Multiplicative noise removal for texture images based on adaptive anisotropic fractional diffusion equations,” *SIAM Journal on Imaging Sciences*, vol. 12, no. 2, pp. 839–873, 2019.
- [17] M. Gao, B. Kang, X. Feng, W. Zhang, and W. Zhang, “Anisotropic diffusion based multiplicative speckle noise removal,” *Sensors*, vol. 19, no. 14, p. 3164, 2019.
- [18] X. Shan, J. Sun, and Z. Guo, “Multiplicative noise removal based on the smooth diffusion equation,” *Journal of Mathematical Imaging and Vision*, vol. 61, pp. 763–779, 2019.
- [19] G. Chierchia, D. Cozzolino, G. Poggi, and L. Verdoliva, “Sar image despeckling through convolutional neural networks,” in *2017 IEEE international geoscience and remote sensing symposium (IGARSS)*. IEEE, 2017, pp. 5438–5441.
- [20] K. Zhang, W. Zuo, Y. Chen, D. Meng, and L. Zhang, “Beyond a gaussian denoiser: Residual learning of deep cnn for image denoising,” *IEEE transactions on image processing*, vol. 26, no. 7, pp. 3142–3155, 2017.
- [21] P. Wang, H. Zhang, and V. M. Patel, “Sar image despeckling using a convolutional neural network,” *IEEE Signal Processing Letters*, vol. 24, no. 12, pp. 1763–1767, 2017.
- [22] S. Baraha and A. K. Sahoo, “Sar image despeckling using plug-and-play admm,” *IET Radar, Sonar & Navigation*, vol. 14, no. 9, pp. 1297–1309, 2020.
- [23] C. U. Mendes, L. Denis, C. Deledalle, and F. Tupin, “Robustness to spatially-correlated speckle in plug-and-play polsar despeckling,” *IEEE Transactions on Geoscience and Remote Sensing*, 2024.
- [24] S. Baraha and A. K. Sahoo, “Plug-and-play priors enabled sar image inpainting in the presence of speckle noise,” in *2020 IEEE 17th India Council International Conference (INDICON)*. IEEE, 2020, pp. 1–6.
- [25] H. Shen, M. Jiang, J. Li, C. Zhou, Q. Yuan, and L. Zhang, “Coupling model-and data-driven methods for remote sensing image restoration and fusion: Improving physical interpretability,” *IEEE Geoscience and Remote Sensing Magazine*, vol. 10, no. 2, pp. 231–249, 2022.
- [26] H. Shen, C. Zhou, J. Li, and Q. Yuan, “Sar image despeckling employing a recursive deep cnn prior,” *IEEE Transactions on Geoscience and Remote Sensing*, vol. 59, no. 1, pp. 273–286, 2020.
- [27] C. Chen, L. Chen, X. Jiang, X. Liu, and A. M. Zoubir, “Deep unrolling network for sar image despeckling,” in *ICASSP 2024-2024 IEEE International Conference on Acoustics, Speech and Signal Processing (ICASSP)*. IEEE, 2024, pp. 4085–4089.
- [28] G. Zhou, Z. Xu, Y. Fan, Z. Zhang, B. Zhang, and Y. Wu, “Deep unfolding network for sparse sar imaging based on compound regularization,” in *IET International Radar Conference (IRC 2023)*, vol. 2023. IET, 2023, pp. 3536–3540.
- [29] S. Mei, J. Lian, X. Wang, Y. Su, M. Ma, and L.-P. Chau, “A comprehensive study on the robustness of deep learning-based image classification and object detection in remote sensing: Surveying and benchmarking,” *Journal of Remote Sensing*, vol. 4, p. 0219, 2024.
- [30] I. J. Goodfellow, J. Shlens, and C. Szegedy, “Explaining and harnessing adversarial examples,” *arXiv preprint arXiv:1412.6572*, 2014.
- [31] A. Kurakin, I. J. Goodfellow, and S. Bengio, “Adversarial examples in the physical world,” in *Artificial intelligence safety and security*. Chapman and Hall/CRC, 2018, pp. 99–112.
- [32] A. Madry, “Towards deep learning models resistant to adversarial attacks,” *arXiv preprint arXiv:1706.06083*, 2017.
- [33] J. Ning, J. Sun, Y. Li, Z. Guo, and W. Zuo, “Evaluating similitude and robustness of deep image denoising models via adversarial attack,” *arXiv preprint arXiv:2306.16050*, 2023.
- [34] H. Yan, J. Zhang, J. Feng, M. Sugiyama, and V. Y. Tan, “Towards adversarially robust deep image denoising,” *arXiv preprint arXiv:2201.04397*, 2022.
- [35] A. Madry, A. Makelov, L. Schmidt, D. Tsipras, and A. Vladu, “Towards deep learning models resistant to adversarial attacks,” *stat*, vol. 1050, no. 9, 2017.
- [36] A. Shafahi, M. Najibi, M. A. Ghiasi, Z. Xu, J. Dickerson, C. Studer, L. S. Davis, G. Taylor, and T. Goldstein, “Adversarial training for free!” *Advances in neural information processing systems*, vol. 32, 2019.
- [37] A. M. Oberman and J. Calder, “Lipschitz regularized deep neural networks converge and generalize,” *arXiv preprint arXiv:1808.09540*, 2018.
- [38] L. Bungert, R. Raab, T. Roith, L. Schwinn, and D. Tenbrinck, “Clip: Cheap lipschitz training of neural networks,” in *International Conference on Scale Space and Variational Methods in Computer Vision*. Springer, 2021, pp. 307–319.
- [39] A. Virmaux and K. Scaman, “Lipschitz regularity of deep neural networks: analysis and efficient estimation,” *Advances in Neural Information Processing Systems*, vol. 31, 2018.
- [40] H. Gouk, E. Frank, B. Pfahringer, and M. J. Cree, “Regularisation of neural networks by enforcing lipschitz continuity,” *Machine Learning*, vol. 110, pp. 393–416, 2021.
- [41] K. Roth, Y. Kilcher, and T. Hofmann, “Adversarial training is a form of data-dependent operator norm regularization,” *Advances in Neural Information Processing Systems*, vol. 33, pp. 14973–14985, 2020.
- [42] S. Aziznejad, H. Gupta, J. Campos, and M. Unser, “Deep neural networks with trainable activations and controlled lipschitz constant,” *IEEE Transactions on Signal Processing*, vol. 68, pp. 4688–4699, 2020.
- [43] Y. Liang and D. Huang, “Large norms of cnn layers do not hurt adversarial robustness,” in *Proceedings of the AAAI Conference on Artificial Intelligence*, vol. 35, no. 10, 2021, pp. 8565–8573.
- [44] L. Cheng, Y. Xing, Y. Li, and Z. Guo, “A diffusion equation for improving the robustness of deep learning speckle removal model,” *Journal of Mathematical Imaging and Vision*, pp. 1–21, 2024.
- [45] L. I. Rudin, S. Osher, and E. Fatemi, “Nonlinear total variation based noise removal algorithms,” *Physica D: nonlinear phenomena*, vol. 60, no. 1–4, pp. 259–268, 1992.
- [46] M. V. Afonso, J. M. Bioucas-Dias, and M. A. Figueiredo, “Fast image recovery using variable splitting and constrained optimization,” *IEEE transactions on image processing*, vol. 19, no. 9, pp. 2345–2356, 2010.
- [47] S. V. Venkatakrisnan, C. A. Bouman, and B. Wohlberg, “Plug-and-play priors for model based reconstruction,” in *2013 IEEE global conference on signal and information processing*. IEEE, 2013, pp. 945–948.
- [48] M. Jetta, U. Singh, and P. Yinukula, “On trainable multiplicative noise removal models,” in *International Conference on Scale Space and Variational Methods in Computer Vision*. Springer, 2023, pp. 81–93.
- [49] C. Szegedy, “Intriguing properties of neural networks,” *arXiv preprint arXiv:1312.6199*, 2013.
- [50] L. C. Evans, *Partial differential equations*. American Mathematical Society, 2022, vol. 19.
- [51] X.-C. Tai, J. Hahn, and G. J. Chung, “A fast algorithm for euler’s elastica model using augmented lagrangian method,” *SIAM Journal on Imaging Sciences*, vol. 4, no. 1, pp. 313–344, 2011.
- [52] R. Zeyde, M. Elad, and M. Protter, “On single image scale-up using sparse-representations,” in *Curves and Surfaces: 7th International Conference, Avignon, France, June 24-30, 2010, Revised Selected Papers 7*. Springer, 2012, pp. 711–730.
- [53] L. Zhang, X. Wu, A. Buades, and X. Li, “Color demosaicking by local directional interpolation and nonlocal adaptive thresholding,” *Journal of Electronic imaging*, vol. 20, no. 2, pp. 023016–023016, 2011.
- [54] M. Rahmehoonfar, T. Chowdhury, A. Sarkar, D. Varshney, M. Yari, and R. Murphy, “Floodnet: A high resolution aerial imagery dataset for post flood scene understanding,” *arXiv preprint arXiv:2012.02951*, 2020.
- [55] G. Cheng, J. Han, and X. Lu, “Remote sensing image scene classification: Benchmark and state of the art,” *Proceedings of the IEEE*, vol. 105, no. 10, pp. 1865–1883, 2017.
- [56] S. Ioffe, “Batch normalization: Accelerating deep network training by reducing internal covariate shift,” *arXiv preprint arXiv:1502.03167*, 2015.
- [57] C.-A. Deledalle, L. Denis, S. Tabti, and F. Tupin, “Mulog, or how to apply gaussian denoisers to multi-channel sar speckle reduction?” *IEEE Transactions on Image Processing*, vol. 26, no. 9, pp. 4389–4403, 2017.
- [58] R. K. Thakur and S. K. Maji, “Agsdnet: Attention and gradient-based sar denoising network,” *IEEE Geoscience and Remote Sensing Letters*, vol. 19, pp. 1–5, 2022.
- [59] M. V. Perera, W. G. C. Bandara, J. M. J. Valanarasu, and V. M. Patel, “Transformer-based sar image despeckling,” in *IGARSS 2022-2022 IEEE International Geoscience and Remote Sensing Symposium*. IEEE, 2022, pp. 751–754.